



### **Science Arts & Métiers (SAM)**

is an open access repository that collects the work of Arts et Métiers Institute of Technology researchers and makes it freely available over the web where possible.

This is an author-deposited version published in: <https://sam.ensam.eu>  
Handle ID: [.http://hdl.handle.net/10985/16578](http://hdl.handle.net/10985/16578)

#### **To cite this version :**

Viet-Duc LE, Nicolas SAINTIER, Franck MOREL, Daniel BELLETT, Pierre OSMOND -  
Investigation of the effect of porosity on the high cycle fatigue behaviour of cast Al-Si alloy by X-ray micro-tomography - International Journal of Fatigue - Vol. 106, p.24-37 - 2018

Any correspondence concerning this service should be sent to the repository

Administrator : [scienceouverte@ensam.eu](mailto:scienceouverte@ensam.eu)



# Investigation of the effect of porosity on the high cycle fatigue behaviour of cast Al-Si alloy by X-ray micro-tomography

Viet-Duc Le<sup>a,b,c,\*</sup>, Nicolas Saintier<sup>b</sup>, Franck Morel<sup>a</sup>, Daniel Bellett<sup>a</sup>, Pierre Osmond<sup>c</sup>

<sup>a</sup> Arts et Métiers ParisTech, Campus Angers – Laboratoire LAMPA – 2 Bd du Ronceray, 49035 Angers Cedex 1, France

<sup>b</sup> Arts et Métiers ParisTech, Campus Bordeaux – Laboratoire I2M – Esplanade des Arts et Métiers, 33405 TALENCE Cedex, France

<sup>c</sup> PSA Peugeot Citroën, 18 rue des fauvelles, 92256 La Garenne-Colombes cedex, France

## Keywords:

Cast aluminium alloy

Fatigue

Tomography

Porosity

Finite element simulation

## A B S T R A C T

Porosity generated by the casting process has a detrimental effect on the high cycle fatigue strength of cast aluminium alloys. The current study presents an investigation using the non-destructive X-ray micro-tomography technique of the effect of the size and the population of casting pores on the fatigue strength of the AlSi7Mg0.3 alloy. This alloy was obtained by the lost foam casting process, which leads to a “high” volume fraction of porosity. Observations by micro-tomography, realized on specimens containing fatigue cracks, highlight an important role of the pore distance to the specimen surface in addition to the pore size. In the second part, the local mechanical response around real 3D pores is investigated thanks to finite element models using an elasto-plastic material behaviour law for the aluminium matrix. A critical volume approach based on the Dang Van criterion to predict the fatigue limit is introduced and shows good agreement with the experimental data. The effect of the pore geometry on the Dang Van equivalent stress distribution around individual pores is also investigated.

## 1. Introduction

Cast aluminium alloys are widely used for automotive applications due to their high strength-to-weight ratio and their good castability which allows the manufacturing of components with very complex geometries. However, traditional casting processes usually generate a variety of defects such as pores and oxides. These defects, particularly shrinkage pores, have a detrimental effect on the fatigue strength of cast aluminium alloys [1–3].

The effect of the pore size on the fatigue strength of cast aluminium alloys has been widely studied in the literature [4–11]. In this body of work the pore size has been typically measured via the observation of polished samples or by the inspection of fatigue failure surfaces. However, these techniques only supply two-dimensional information about the pore geometry at the crack initiation site. Because of this limitation, very few studies have investigated the effect of the free surface (i.e. the spatial position of the pores with respect to the specimen surface) and effect of the 3D pore geometry. For instance, in the work of Serrano et al. [12] artificial defects were introduced on the surface (surface defects) and in the bulk (internal defects) of a cast Al-Si-Mg alloy. The authors observed that the specimens with surface defects had a fatigue strength at  $5 \times 10^6$  cycles that was significantly lower

(i.e. 70% lower) than that of the specimens with internal defects. Concerning the effect of the pore geometry, in the work of Houria [13] the fatigue strength of specimens with natural casting pores is compared with the those with artificial semi-spherical surface defects. The author observed that for the same value of the area square root ( $\sqrt{area}$ ) measured on the failure surfaces, there is no difference in the fatigue strength between the artificial defects and natural ones.

Besides these experimental approaches, the fatigue behaviour of cast aluminium alloys has been also investigated by means of the finite element method (FEM). Gao et al. [14] and Fan et al. [15] studied the cyclic behaviour of cast aluminium alloys at the scale of silicon particles in the eutectic zones. Recently, based on X-ray micro-tomography measurements, several studies concerning the influence of casting pores have been conducted using 3D FEM simulations of pores. For instance, Ferri et al. [16,17] and Dezecot et al. [18], studied crack initiation and crack propagation mechanisms from casting pores in the low cycle fatigue regime, thanks to high resolution in-situ micro-tomography observations. In the work by Nicoletto et al. [19,20] and Tijani et al. [21,22], stress concentration factors at casting pores in an aluminium alloy were calculated considering a purely linear elastic behaviour. Vanderesse et al. [23] defined the pore influence zone, the regions in which the von Mises stress is higher than the material 0.2% yield stress,

\* Corresponding author at: Arts et Métiers ParisTech, Campus Angers – Laboratoire LAMPA – 2 Bd du Ronceray, 49035 Angers Cedex 1, France.  
E-mail address: viet-duc.le@ensam.eu (V.-D. Le).

## Nomenclature

$\beta$	macroscopic torsional fatigue strength for $R = -1$ [MPa]
$\hat{\sigma}_{H_i}(t)$	local hydrostatic stress at instant $t$ [MPa]
$\langle \cdot \rangle_r$	calculation of the average value in a spherical volume of radius of $r$
$\Sigma_a$	macroscopic applied stress amplitude [MPa]
$\Sigma_{a,D}$	macroscopic fatigue strength amplitude at $2 \times 10^6$ cycles [MPa]
$\Sigma_{a,nf}$	macroscopic applied stress amplitude level of the final loading step [MPa]
$\sigma_{DV}$	local equivalent Dang Van stress [MPa]
$\hat{\tau}(\underline{n}, t)$	local resolved shear stress applied on the plan with the normal vector $\underline{n}$ at instant $t$ [MPa]
$\underline{\sigma}$	local Cauchy stress tensor at gauss points
$\underline{X}$	kinematic hardening variable
$A$	area of the 3D surface of pores [ $\mu\text{m}^2$ ]

$N_f$	number of cycles corresponding to the failure of the specimen
$R$	isotropic hardening variable [MPa]
$r$	radius of the spherical volume for calculating the average value [ $\mu\text{m}$ ]
$R_0$	initial yield strength under the uniaxial tensile loads [MPa]
$V$	volume of the pores [ $\mu\text{m}^3$ ]
$V_r$	volume of the sphere of radius of $r$ for calculating average values [ $\mu\text{m}^3$ ]
$b$	ajustement parameter of the stabilisation rate
DV	Dang Van fatigue danger indicator
$p$	accumulated plastic strain
$Q$	asymptotic value corresponding to the stabilised cyclic regime [MPa]

to correlate with the location of the crack starting point.

In summary, to the authors knowledge the effect of the distance between a casting pore and the free surface has not yet been clearly investigated in the literature. Also, the results obtained from FEM simulations of real 3D pore geometries in the High Cycle Fatigue (HCF) regime have been limited to the estimation of stress concentration factors. No real approach to estimate the high cycle fatigue strength based on real 3D pore geometries has been proposed.

In the first part of this paper, the influence of the pore population on the high cycle fatigue behaviour of a cast Al-Si alloy is investigated using the micro-tomography technique. More exactly, the role of the spatial position of each pore to the free surface on the fatigue strength is studied. This aspect is evaluated by the extensive use of micro-tomography in order to precisely determine the characteristics of the critical defect population compared to the whole defect population. In the second section, FEM simulations are presented to analyse the stress distribution around casting pores. In these simulations, an elasto-plastic material behaviour law including non-linear isotropic and kinematic hardening is used for the aluminium matrix. This law is identified thanks to the results obtained from cyclic hardening tests. Based on the results of the FEM simulations, a critical volume approach based on the Dang Van criterion is proposed to estimate the high cycle fatigue strength. The effect of the 3D pore geometry is also investigated via the comparison of the Dang Van equivalent stress for natural casting pores and artificial pores with different simplified geometries.

## 2. Materials and fatigue tests

In two previous publications [10,11], the authors have presented the results of experimental work investigating the high cycle multiaxial fatigue behaviour of three cast aluminium alloys, referred to as alloys A, B and C. The fabrication steps of the three alloys are as follows.

- Alloy A: gravity die casting followed by a standard T7 heat treatment
- Alloy B: lost foam casting followed by a standard T7 heat treatment
- Alloy C: lost foam casting followed by Hot Isostatic Pressing (HIP) and then a T7 heat treatment

In the present study, the effect of porosity on the fatigue strength is investigated only on alloy B. However, alloy C, subjected to an HIP post-treatment and hence considered to be porosity-free, is used to identify the cyclic hardening behaviour that is used in FEM simulations of alloy B. It is then considered that the HIP treatment has no effect on the microstructure of the material apart from closing the pores. The micrography of the two materials suggest that the HIP treatment has effectively a low impact on the microstructure (similar SDAS) These aspects will be further detailed in the following sections.

### 2.1. Alloy B and high cycle fatigue behaviour

This AlSi7Mg0.3 alloy, was produced by lost foam die casting in the form of plates, 200 mm  $\times$  150 mm  $\times$  18 mm in size. The material was then subjected to a T7 post-casting heat treatment. This casting process

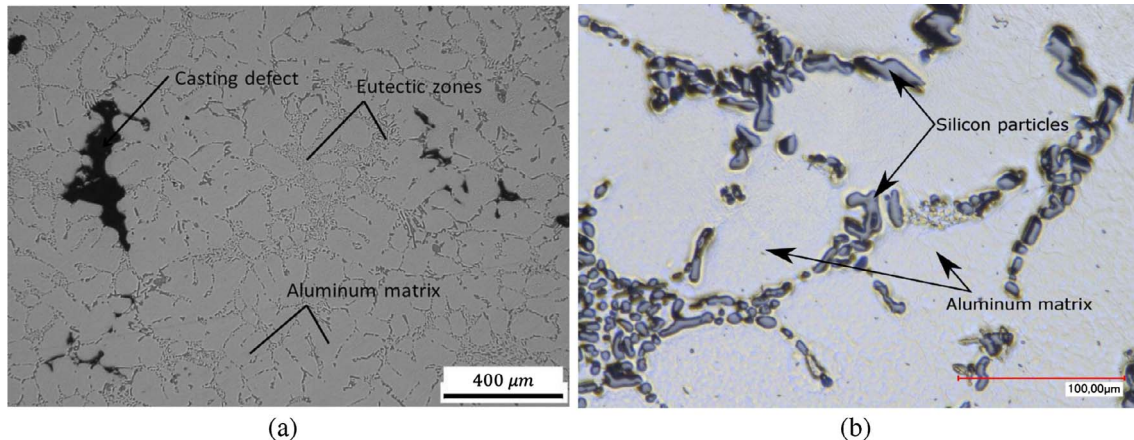


Fig. 1. Microstructural heterogeneities present in the cast aluminium alloys under investigation AlSi7Mg0.3: (a) typical microstructure of cast aluminium alloys; (b) zoomed view [10].

leads to a material with relatively high porosity volume fraction (0.28% estimated by micro-tomography measures). Fig. 1 shows typical microstructural images of the aluminium alloy under investigation.

This alloy has an ultimate tensile strength of  $\sigma_{UTS} = 251$  MPa, a yield strength of  $\sigma_{Y0.2\%} = 240$  MPa, a Young's modulus of  $E = 68$  GPa, and an elongation at fracture of  $A = 0.8\%$ . Monotonic tensile tests were conducted on cylindrical specimens with a gauge length of 30 mm and a gauge diameter of 5 mm. Concerning the properties of the aluminium matrix, alloy B has an average SDAS of 77  $\mu\text{m}$  and a micro-hardness of 99 HV025 with a standard deviation of 9 HV025. Plain fatigue specimens with a circular cross-section of diameter 7 mm and a gauge length of 15 mm were used (Fig. 5(a)). The gage length of the specimens was mirror polished in order to evaluate the effect of microstructure and defects on the fatigue strength and eliminate the impact of specimen machining.

The fatigue tests were conducted using a Rumul resonance testing machine with a  $\pm 10$  kN load cell, at room temperature. Constant-amplitude uniaxial stress-controlled tests were conducted with a stress ratio of  $R = -1$  and a frequency of approximately 80 Hz. The staircase technique with a stress amplitude step of 10 MPa was used to determine the fatigue strength at  $2 \times 10^6$  cycles. The tests were stopped when the presence of a fatigue crack of approximately 3 mm in length was detected via a drop in the resonant frequency. The specimens that survived  $2 \times 10^6$  cycles in the staircase procedure were retested at a stress amplitude one step higher for another  $2 \times 10^6$  cycles. This was repeated until failure of the specimen at less than  $2 \times 10^6$  cycles. For this alloy (alloy B) 21 specimens were tested and the results are shown in Table 1. The number of cycles to failure corresponding to the final stress level,  $N_f$ , and the defect size at the crack initiation site observed on the failure surfaces,  $\sqrt{area}$ , are also reported. The main advantage of this testing method is that the fatigue behaviour of the material, including the average fatigue strength and the associated scatter, can be determined using the staircase data (i.e. the black coloured data in the staircase table). The mean fatigue strength is determined to be  $\Sigma_{a,D} = 62$  MPa and the standard deviation is estimated to be 12 MPa. The fatigue strength of each specimen was also estimated by the LOCATI method (see Section 4.3 below).

## 2.2. Alloy C and identification of the cyclic hardening behaviour

In order to properly evaluate the local stress/strain fields by FEM simulations around the defects of alloy B, an elasto-plastic constitutive model is required to simulate the mechanical response of the aluminium microstructure (i.e. the  $\alpha$  phase dendrites and the eutectic zones). Because of the high fraction of porosity in alloy B, it was decided to use the cyclic hardening behaviour of alloy C. Note that alloy C, has the

same chemical composition as alloy B and that it is obtained by lost foam casting, followed by Hot Isostatic Pressing (HIP) and then a conventional T7 heat treatment. The maximum defect size,  $\sqrt{area}$ , observed by optical microscopy in alloy C is smaller than 50  $\mu\text{m}$ , compared to an average defect size of 470  $\mu\text{m}$  in alloy B. Hence, alloy C is considered to be porosity-free. Alloy C has a tensile strength of  $\sigma_{UTS} = 275$  MPa, a yield strength of  $\sigma_{Y0.2\%} = 250$  MPa, a Young's modulus of  $E = 74$  GPa and an elongation at fracture of  $A = 2.3\%$ . The fatigue strength corresponding to a failure probability of 50% under uniaxial loading conditions with a load ratio of  $R = -1$  and at  $2 \times 10^6$  cycles is  $\Sigma_{a,D} = 126$  MPa. In particular, SDAS and micro micro-hardness of alloy C are close to those of alloy B. It is therefore expected that the macroscopic cyclic hardening behaviour of alloy C will be the same as that of the aluminium matrix of alloy B ( $\alpha$ -Al phase and eutectic phase).

Imposed total strain cyclic hardening tests on specimen of alloy C have been conducted with a load ratio of  $R = -1$  at a constant strain rate of  $0.004 \text{ s}^{-1}$ . Three imposed strain amplitude levels have been applied: 0.30%, 0.42% and 0.50%. Fig. 2a–c shows the cyclic behaviour for these three imposed strain levels for different numbers of cycles.

The cyclic hardening behaviour of alloy C is decomposed using 4 hardening variables,  $X_a, R_a, \Sigma_{eq,a}, \Sigma_{eq,m}$  as introduced in the work of Feaugas et al. [24]. These variables are given by Eq. (1) and schematically given in Fig. 2(d) for each full cycle. The classical von Mises yield function is used to describe the yield surface. The yield stress is determined using a plastic strain threshold of  $2 \times 10^{-4}$ .

$$\begin{aligned} X_a &= \frac{X^+ + |X^-|}{2} \\ R_a &= \frac{R^+ + |R^-|}{2} \\ \Sigma_{eq,a} &= \frac{\Sigma_{max}^+ + |\Sigma_{min}^-|}{2} \\ \Sigma_{eq,m} &= \frac{\Sigma_{max}^- + |\Sigma_{min}^-|}{2} \end{aligned} \quad (1)$$

The evolution of these variables as a function of the number of cycles is shown in Fig. 3 for different imposed strain amplitudes.

It can be observed that the stabilisation of the cyclic behaviour is reached very quickly (after approximately 10 cycles) and that the evolution of the isotropic hardening is negligible for all applied strain levels. It can therefore be concluded that the cyclic behaviour of the alloy C is not characterized by significant cyclic hardening or softening.

In order to model the cyclic hardening behaviour of alloy A, the Lemaitre and Chaboche [25] non-linear isotropic and kinematic hardening constitutive equations were chosen. The isotropic and kinematic hardening are described by the following expressions.

$$R = R_0 + Q \left( 1 - \frac{1}{e^{bp}} \right) \quad (2)$$

**Table 1**

Fatigue test result of alloy B presented in the form of stair-case table. O = specimens survived  $2 \times 10^6$  cycles. X = specimens failure at a  $N_f$  cycles.

N° Sp.	1	2	3	4	5	6	7	8	9	10	11	12	13	14	15	16	17	18	19	20	21
$\Sigma_a$ [MPa]																					
80			X	X						O					X	X			X		X
70	X	X	O		X			X		O	X	X	X	X	O		X	X	O		O
60		O				X		O	X	O		O	O					O		X	O
50							X	O	O												O
40								O													
$N_f(\times 10^6)$	0.66	0.82	1.62	1.07	0.82	1.90	1.79	1.58	1.80	N/A	1.39	1.10	0.40	0.35	0.65	1.06	1.09	1.60	0.63	1.58	1.37
$\sqrt{area}$ [ $\mu\text{m}$ ]	1212	411	379	407	1064	906	970	387	648	N/A	485	526	342	604	328	423	479	N/A	446	664	616

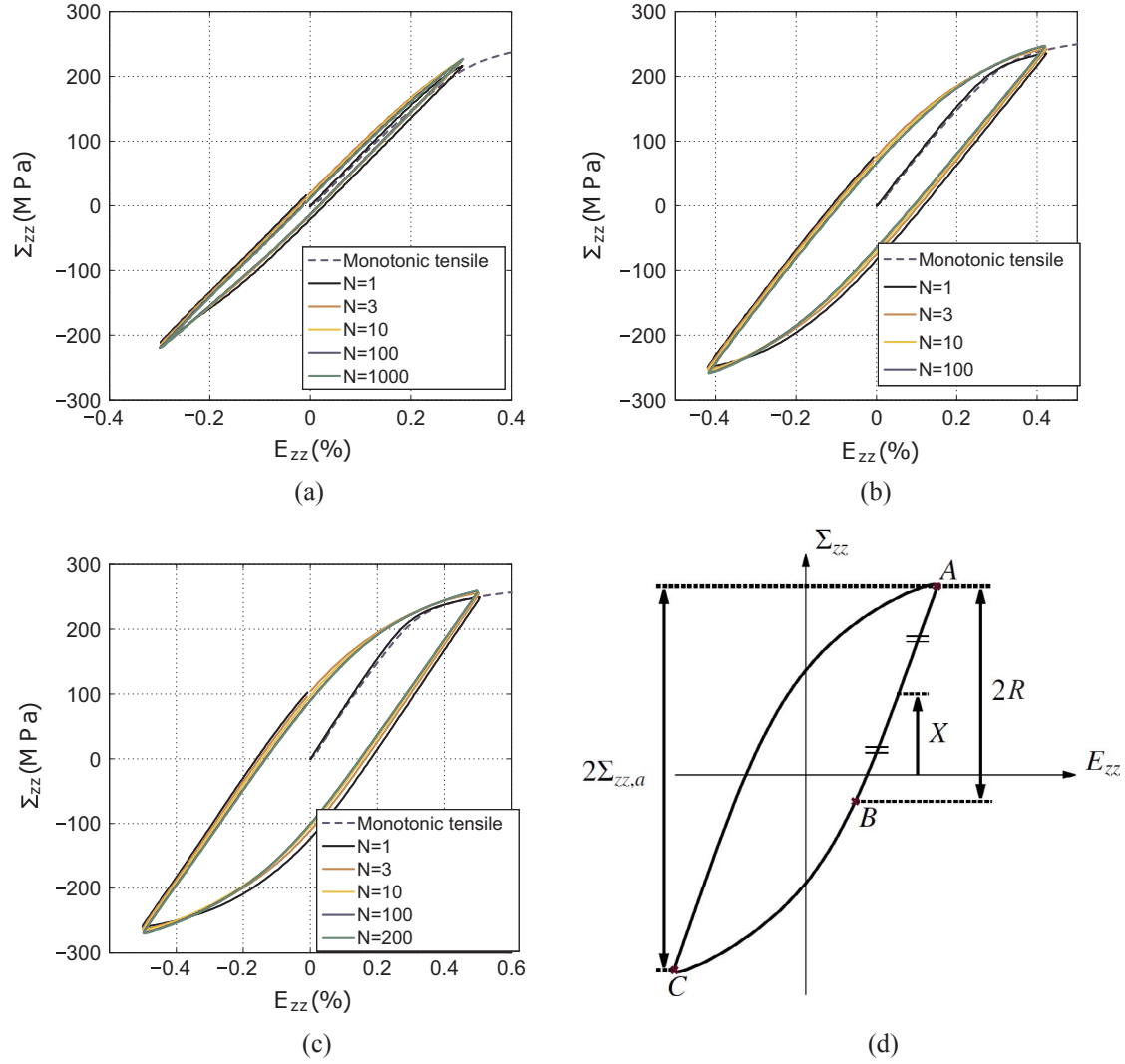


Fig. 2. Stress-strain loops corresponding to a total strain amplitude of 0.30% (a), 0.42% (b), 0.50% (c) and schema of a uniaxial tension-compression loading cycle showing the isotropic and kinematic hardening contributions (d).

$$\underline{\dot{X}} = \frac{2}{3} C \underline{\dot{\epsilon}}^p - D \underline{X} \dot{p} \quad (3)$$

These parameters were identified by the Levenberg Marquardt optimization algorithm implemented in the ZeBuLoN finite element code. The optimised numerical values are shown in Table 2.

Fig. 4 shows the comparison between the experimental stress-strain curves and the model predictions for the first cycle a good agreement can be seen. In the FEM simulations presented in the next sections, all the simulations have been carried out for only 1 cycle.

### 3. Non-destructive testing by X-ray microtomography on alloy B

Measurements using the X-ray micro-tomography technique were conducted at the PLACAMAT (attached to the University of Bordeaux and CNRS), in France on a microtomograph X GE V/TOME/SX. A spatial resolution of  $5 \mu\text{m} \times 5 \mu\text{m} \times 5 \mu\text{m}$  was used with a 160 kV (max) X-ray source. The obtained data were reconstructed and analysed with the Avizo® software.

Because of the large size of the fatigue specimens (diameter = 7 mm, gauge length = 15 mm), it was not possible to carry out in-situ fatigue tests. Consequently, it was decided to scan each specimen only once, after being tested in fatigue, in the zone containing the principal fatigue crack. Note that the crack length is approximately 3 mm on surface. The scanned volume covers the complete cross section

of the specimen with a length of 8 mm so that a large amount of critical configuration could be captured. Fig. 5(b) shows schematically the size and the position of the volume observed by micro-tomography on the specimens tested in fatigue.

In total, 7 alloy B specimens taken from the 21 specimens tested in fatigue by the staircase technique (see Table 1 in Section 2) were observed by micro-tomography. Table 3 regroups the results of the fatigue tests on these specimens.

In order to distinguish the cracks and the pores causing crack initiation in the tomography images, different grey level thresholds were used. Fig. 6 shows 3D renderings of a principal crack and the pore at the origin of crack initiation.

The size, in terms of volume, and the spatial position of all pores in the scanned volume have been subsequently measured. Note that pores with a size smaller than  $15 \mu\text{m}$  ( $V^{1/3} < 15 \mu\text{m}$ ) were disregarded in the analysis. Effectively this limit corresponds to the numerical noises produced in the image scanning or image post-treating process. It is also expected that the influence of such small pores on the fatigue strength of the cast aluminium alloy is likely to be negligible [4,5,8,10].

#### 3.1. Defect population

The volume and the maximum feret diameter are measured for each pore. In order to obtain a representative distribution of the pore size,

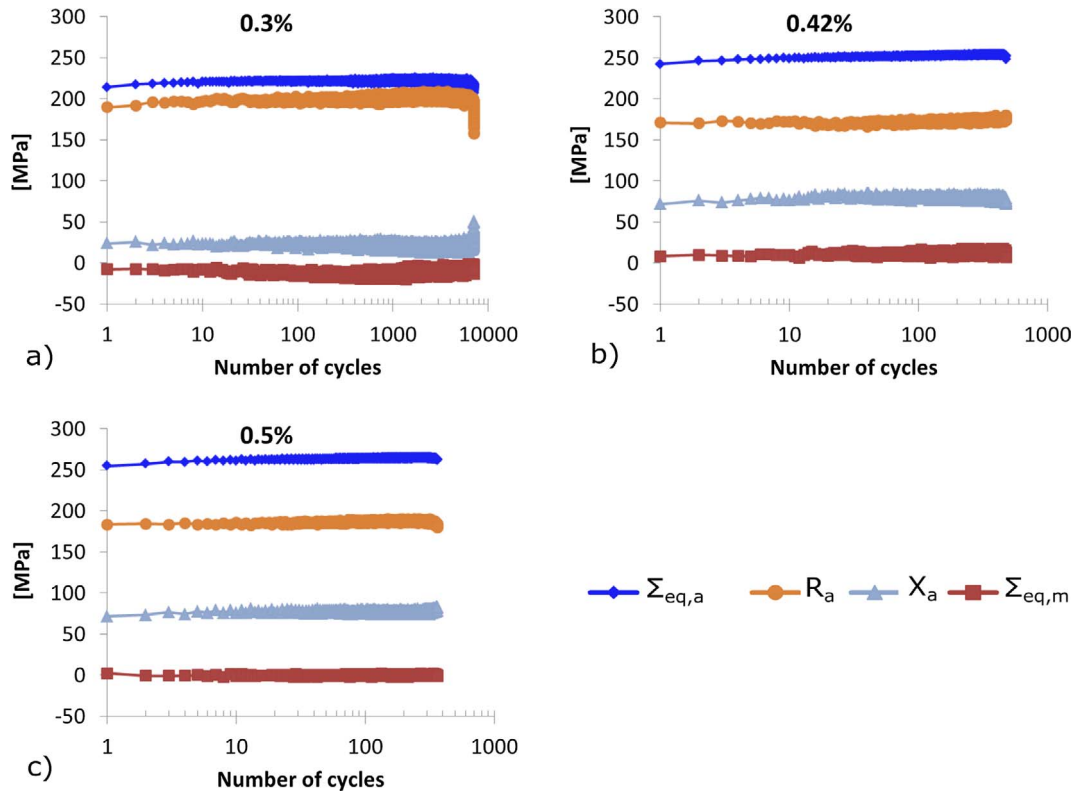


Fig. 3. Evolution of the stress amplitude, of the mean stress, of the kinematic hardening and of the isotropic hardening as a function of the cycle number for alloy C.

Table 2  
The optimised elasto-plastic parameters obtained for alloy C.

Parameter	E [GPa]	$R_0$ [MPa]	b	Q [MPa]	C [GPa]	D [GPa]
Value	75.5	170	19	20	127.5	1.3

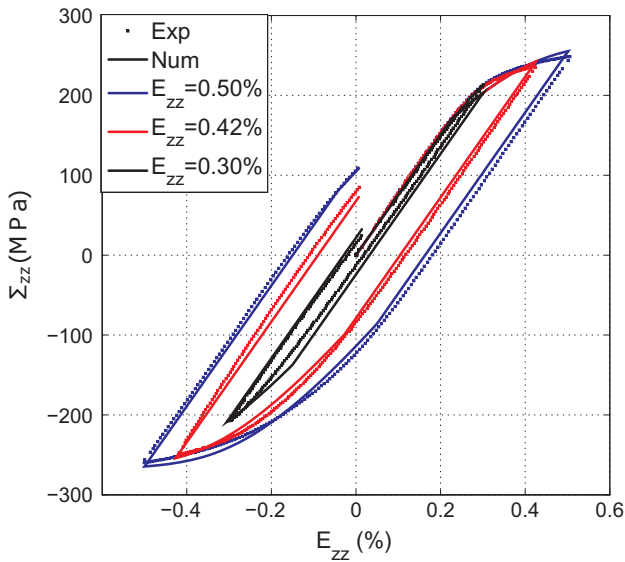


Fig. 4. Comparison of the experimental cyclic hardening behaviour for alloy C and the simulation for the cycle  $N = 1$ .

the data obtained from the 7 scanned specimens have been regrouped and treated as a unique data set. The pore size distributions from all the observed specimens are presented in Fig. 7. These distributions correspond hence to a total scanned volume of  $2.16 \times 10^3 \text{ mm}^3$ .

The distributions show that the fraction in number of large pores is very small and that the lognormal distribution is not a good fit for the large pores. It can also be seen that the feret diameter of the largest pores is 5 to 10 times greater than the volume cube root (for comparison, this factor is 1.24 for a perfectly spherical pore). This implies that the largest casting pores have very torturous shapes. In order to characterize the pore tortuosity, the sphericity of the pores, defined by Eq. (4), is analysed. A small sphericity value correspond to the pores with high tortuosity. The maximum value of the sphericity is 1 corresponding to a perfectly spherical pores.

$$\text{Sphericity} = \frac{\pi^{1/3}(6V)^{2/3}}{A} \quad (4)$$

where  $V$  is the pore volume and  $A$  is the pore surface area.

Fig. 8 shows the relationship between the sphericity and the pore volume cube root.

It can be seen that as a general rule the pore volume decreases when the sphericity increases. In other words, the large pores are more tortuous than the small pores. This is because of the presence of different kinds of porosity (i.e. shrinkage and gaseous cavities).

### 3.2. Effect of the distance from the pore to the specimen surface on fatigue crack initiation

In previous work concerning the HCF behaviour of cast aluminium alloys conducted by the Arts et Métiers ParisTech research team [1,7,10], it has been shown that the principal fatigue cracks leading to final failure of the specimens initiated systematically from pores located on the specimen surface or sub-surface. No crack initiation from internal pores has been observed.

In order to better understand the role of the distance from a pore to the specimen surface on crack initiation process, the size (in terms of  $V^{1/3}$ ) and the distance to the specimen surface for all of the pores in the scanned volumes are analysed. Note that the distance to the surface is defined as the shortest distance from the pore centroid to the specimen

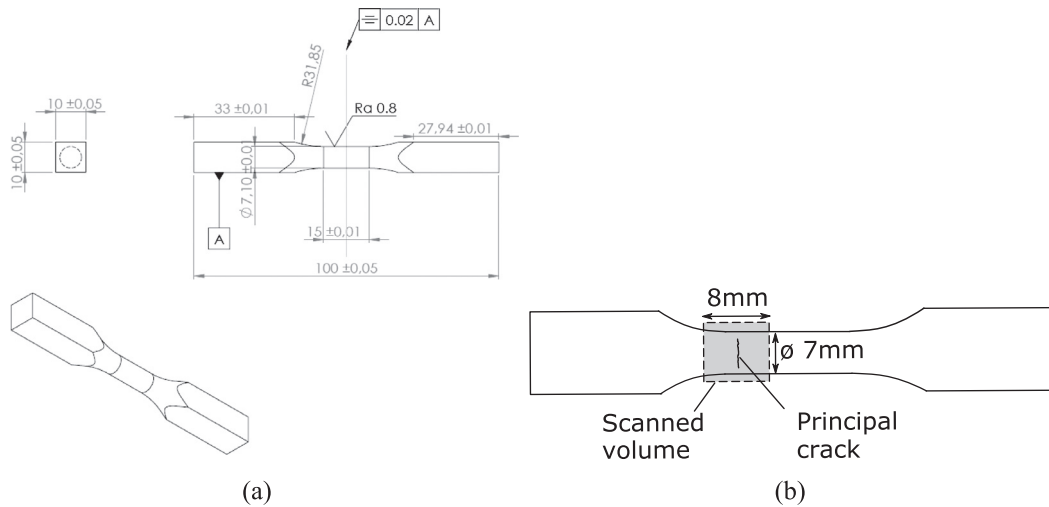


Fig. 5. (a) Fatigue specimen; (b) Scanned volume by micro-tomography on the fatigue tested specimens.

Table 3

Summary of 7 specimens tested in fatigue and subsequently scanned via micro-tomography. O = the specimen survived  $2 \times 10^6$  cycles. X = specimen failure at a  $N_f$  cycles.

Stress amplitude $\Sigma_a$ [MPa]	Specimen number						
	11	12	14	17	19	20	21
80					X		X
70	X	X	X	X	O		O
60		O	O			X	O
50							O
$N_f$ ( $\times 10^6$ ) [cycles]	1.39	1.10	0.35	1.09	0.63	1.58	1.37
Critical defect size $\sqrt{area}$ [ $\mu\text{m}$ ]	485	526	604	479	446	664	616

surface.

Fig. 9 shows the “distance to surface versus pore size” and “sphericity versus pore size” diagrams for the 7 scanned specimens (the specimen numbers are indicated in Table 3) as well as diagrams superposing the results for all 7 specimens.

In these figures each point corresponds to a pore. The open points represent the pores not associated with crack initiation. The large filled points are the pores associated with principal crack initiation and the small filled points represent the secondary cracks. The distinction between the principal crack and the secondary cracks is based on the crack size observed by micro-tomography. Only secondary cracks located far enough away from the principal crack are reported so that it can be assumed that the presence of the principal crack did not affect initiation of the secondary cracks. Table 4 summarizes the size and the distance to specimen surface of the pores causing crack initiation and of

the largest pore observed in each specimen.

It can be seen that for specimens 11, 12, 17 and 19 the largest pores in the observed volumes do not result in crack initiation. In these specimens, the largest pores are located closer to the center of the observed volumes while the pores causing crack initiation are near the specimen surface and are smaller. Furthermore, it is generally observed that all the pores initiating the fatigue cracks are located near the specimen surface with a distance to the surface that is less than  $500 \mu\text{m}$ . By examining the raw images from the micro-tomography scans, it is observed that there is no sub-surface crack initiation. All of the pores causing crack initiation intersect with the specimen surface, as illustrated in Fig. 10. There are two possible explanations for this phenomenon. Firstly, a higher stress concentration is likely to be generated at a surface or sub-surface pore compared to the same pore morphology located in the bulk material [21,22,26]. The second possible reason is that due to environmental effects cracks initiating from surface pores have a higher crack growth rate compared to those initiating from internal pores. It has been reported that crack propagation plays a significant role in the high cycle fatigue life of cast aluminium alloys [27]. For cracks initiated from internal pores propagation occurs essentially in a vacuum while for cracks initiating from a surface pore, the propagation takes place in an air environment. In the literature, the beneficial effect of the vacuum on the fatigue life in metallic materials was shown [28]. For cast aluminium alloys Serrano et al. [12] showed that the difference of the crack growth rate between the crack propagation in vacuum and in air is by a factor of 10.

Concerning the role of the pore sphericity, it can be observed that 6 pores at the origin of fatal cracks (out of a total of 7 pores) have a

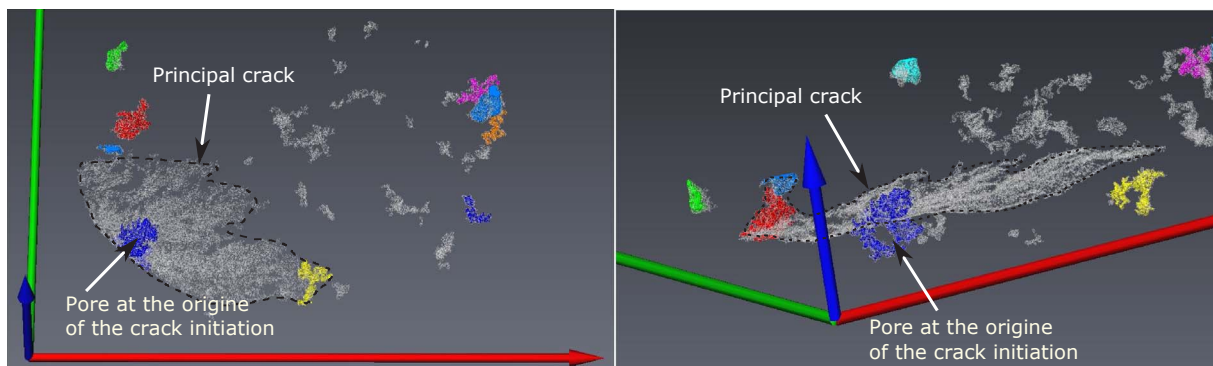
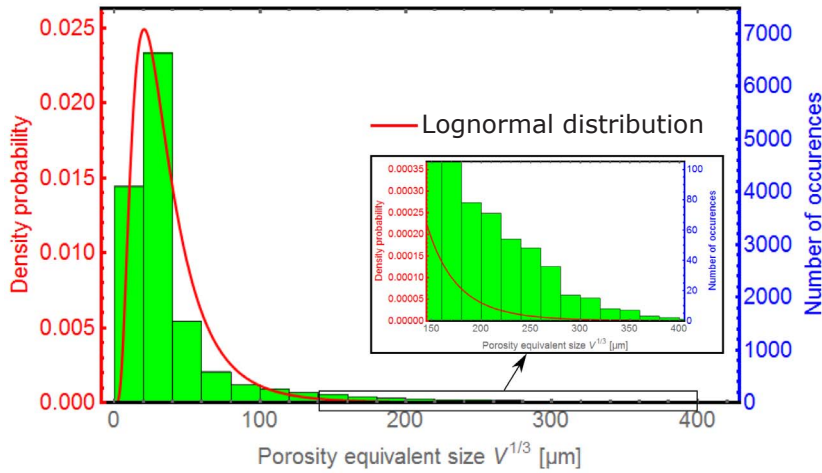
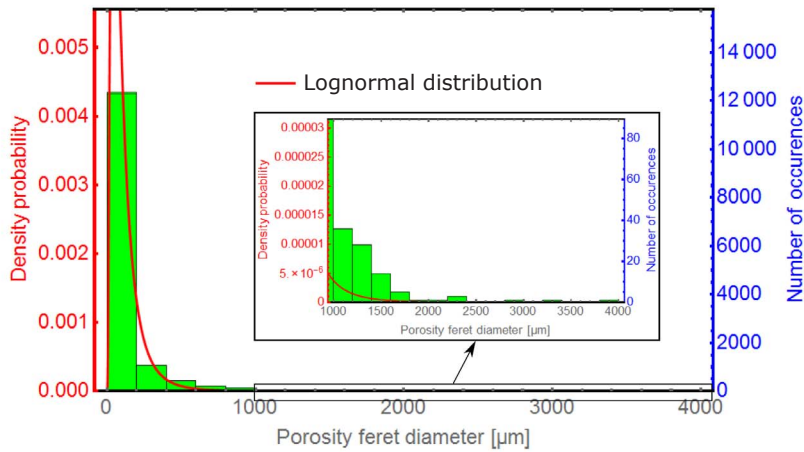


Fig. 6. Two 3D renderings of a principal crack observed on the specimen number 11, tested in fatigue. The pore causing crack initiation is in blue. (For interpretation of the references to colour in this figure legend, the reader is referred to the web version of this article.)

Fig. 7. Pore size distributions for alloy B including zoomed views in the large pore domain.



(a) Histogram of the cube root of the volume ( $V^{1/3}$ ) and the best-fit lognormal curve



(b) Histogram of the feret diameter and the best-fit lognormal curve

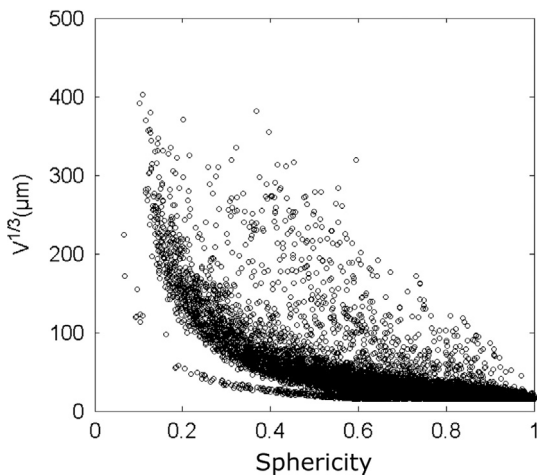


Fig. 8. Sphericity as a function of the volume cube root of the observed pores.

sphericity that is less than 0.2. However, because these pores are also among the largest pores close to the specimen free surface, it is difficult to make a conclusion concerning a threshold value of the sphericity on the initiation of fatal cracks.

#### 4. Finite element simulations of real 3D casting pores in alloy B

Based on the micro-tomography analyses, the numerical geometries of all pores located in the scanned volumes were obtained. Finite element models of the 3D casting pores have been then built and the local mechanical response surrounding the pores is investigated. A fatigue modelling approach is then developed to predict the fatigue strength of the specimens from the results of the FE simulation for critical pores.

##### 4.1. Finite element model

The FE simulations are described in Fig. 11a–d. After generating a surface model of the pores using the Avizo® software, the defects were placed in a cylindrical volume with a diameter of 7 mm and a height of 4–6 mm (Fig. 11b). The size of the simulated volume is chosen to achieve reasonable computation time and to be large enough to avoid border effects (at the upper and lower faces of the cylinder) in the stress field surrounding the pores. The pores are spatially positioned in the modelled volume in their real positions, identified from the micro-tomography observation. The finite element mesh size is approximately 8 μm at the pore surface and 200 μm at the outer surfaces of the cylindrical volume. Linear tetrahedral elements designated “C3D4” are used in the simulations. It is important to note that each simulated volume contains only one pore. The effect of the interaction between pores in the mechanical response is not considered in this study.

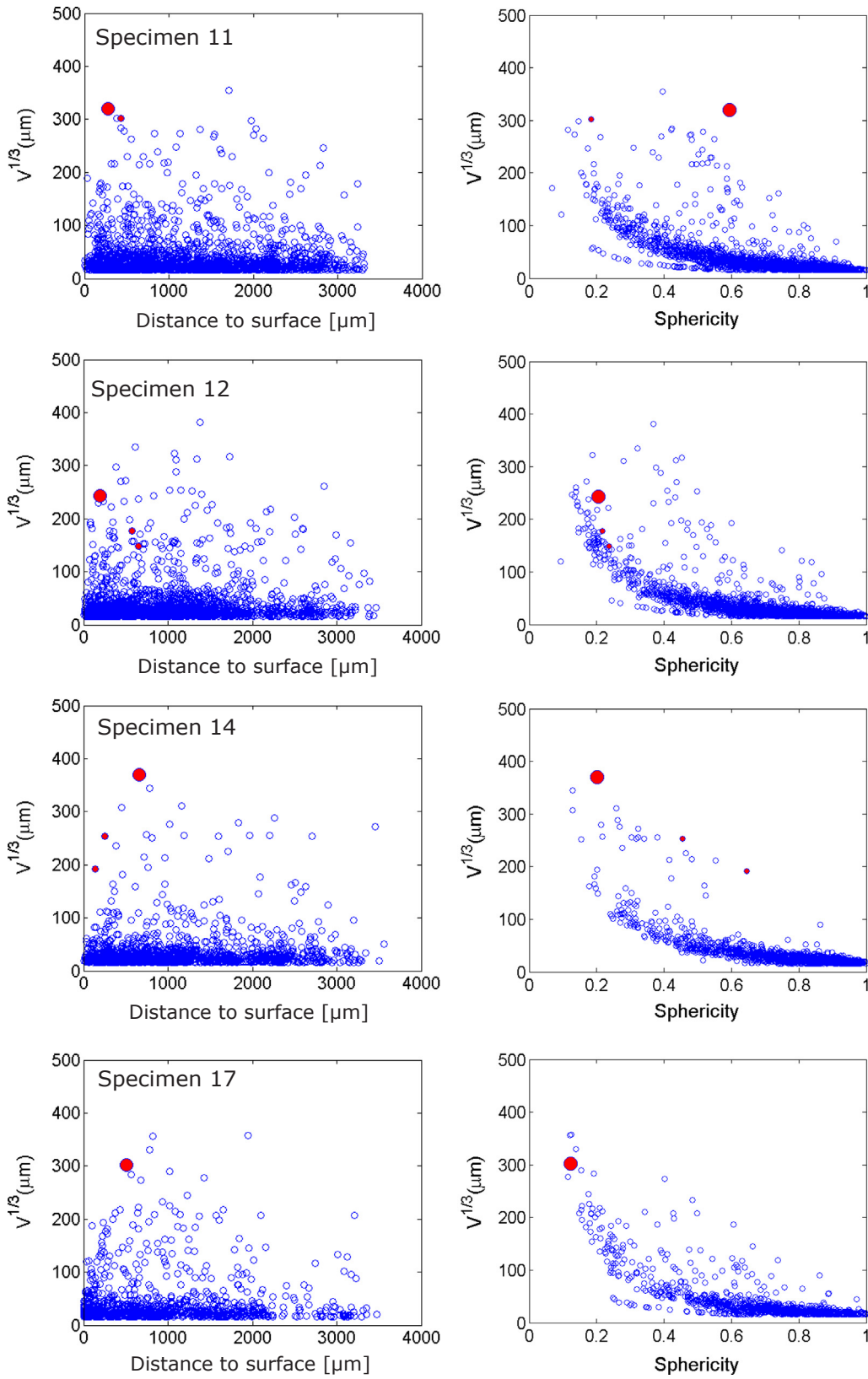
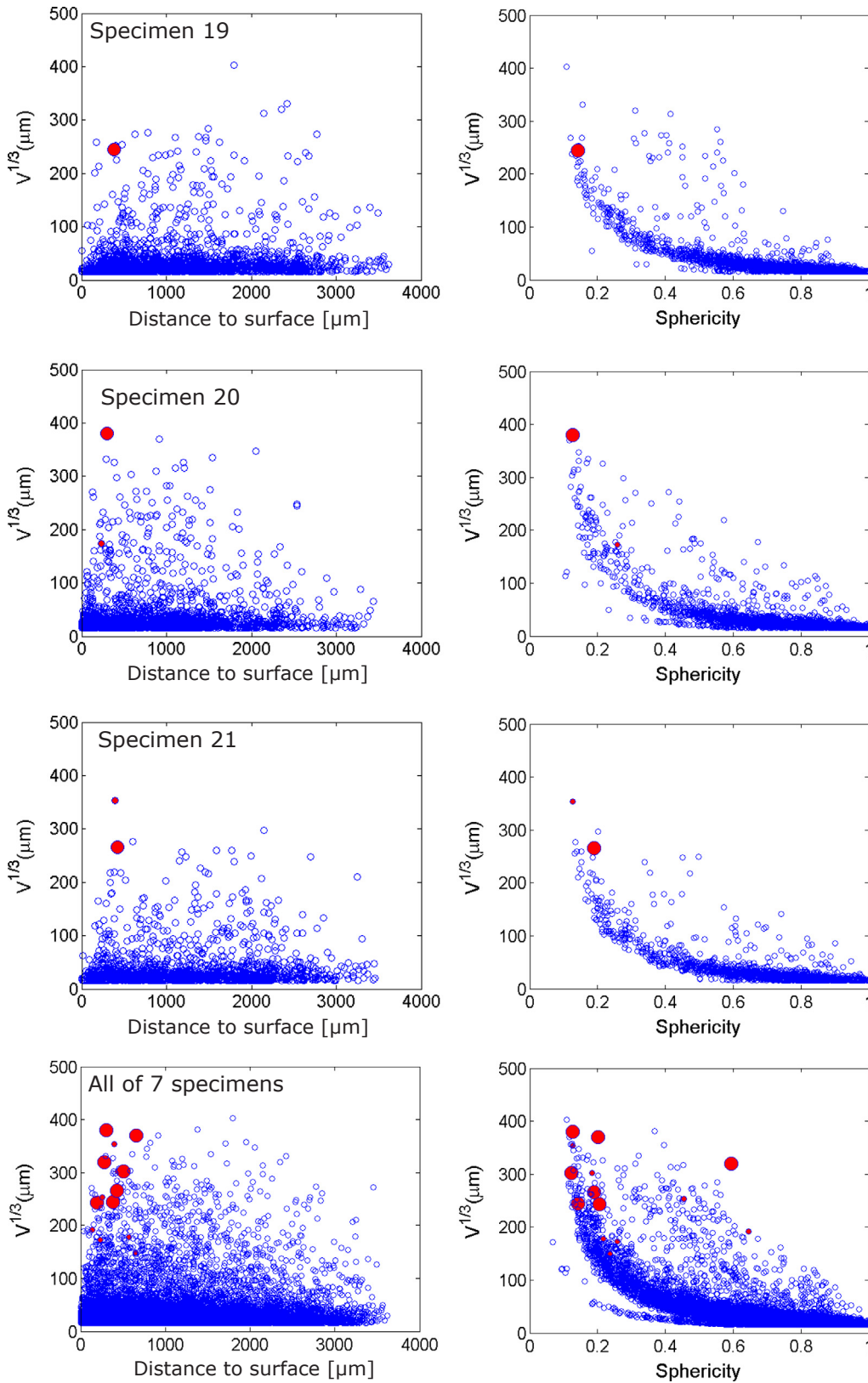


Fig. 9. Size, sphericity and distance to the specimen surface of pores. Open spots: pores not associating to any crack; big full spots: pores associating to the principal cracks; small full spots: pores associating to the secondary cracks.

Fig. 11d shows the boundary conditions applied to the simulated volumes. The numerically applied stress  $\Sigma_a$  is equal the experimentally applied stress level corresponding to failure of the specimens (see

Table 3). Fig. 11e shows an example of a critical pore and the stress field in the axial direction ( $\sigma_{33}$ ) around the pore, without the presence of the fatigue crack. Note that the axial direction is the loading direction

Fig. 9. (continued)



and is noted as  $e_3$  for both the FE models.

#### 4.2. Local mechanical response and a proposed fatigue modelling approach

Based on the critical distance theories developed by Susmel et al. [29] (the line and point methods) and Bellett et al. [30] (the volume method), El may et al. [31] proposed a critical volume approach to

predict the fatigue strength of the X12CrNiMoV12-3 steel containing corrosion pores on the specimen surface. The approach uses the “average value” of the equivalent stress determined using the Crossland criterion, in a spherical volume of radius  $r$ . For the cast Al-Si alloy under investigation, this approach presents two main advantages. Firstly, the effect of the mesh size on the pore surface is strongly reduced. Because of the small pore size ( $V^{1/3} > 150 \mu\text{m}$ ), the FE mesh cannot be

**Table 4**

Summary of pore size ( $v^{1/3}$ ) and the distance to the specimen surface (Dist.) of the largest pore observed in each specimen and the pore causing fatigue crack initiation. Fatigue cracks are classified as either principal cracks (Prin. crack) or secondary cracks (Sec. crack). All values are in  $\mu\text{m}$ .

Sp. N°	Pri. crack		Sec. crack 1		Sec. crack 2		Largest pore	
	$v^{1/3}$	Dist.	$v^{1/3}$	Dist.	$v^{1/3}$	Dist.	$v^{1/3}$	Dist.
11	319	276	302	435	–	–	355	1713
12	243	190	177	573	149	652	382	1381
14	370	657	253	252	191	138	370	657
17	302	507	–	–	–	–	358	1950
19	244	385	–	–	–	–	403	1798
20	380	299	173	235	–	–	380	299
21	266	425	354	395	–	–	354	395

adequately refined to achieve a full convergence of the local stresses. The “average” stress is much less dependent on the element size. The second advantage is that this approach takes into account not only the crack initiation condition but also micro-crack propagation. Because of the important role of crack propagation on the HCF life of cast aluminium alloys, it can be argued that the use of the average value is more reasonable for engineering fatigue design than the local value at the pore surface.

In the present study, the “average” Cauchy stress tensor at gauss point  $i$  centered in a sphere of radius  $r$  and volume  $V_r$  is firstly calculated. The Cauchy stress tensor is “averaged” in the volume  $V_r$  using Eq. (5).

$$\langle \underline{\underline{\sigma}}(t)_i \rangle \Big|_r = \frac{1}{V_r} \int_{V_r} \underline{\underline{\sigma}}(t) dV_r \quad (5)$$

This calculation has been implemented in a finite element code by using the numerical transformation of Eq. (5), given by following expression:

$$\langle \underline{\underline{\sigma}}(t)_i \rangle \Big|_r = \frac{1}{V_r} \sum_{k \in V_r} \underline{\underline{\sigma}}_k(t) \det(J_k) W_k \quad (6)$$

where  $\underline{\underline{\sigma}}_k(t)$  is the Cauchy stress tensor for time  $t$  at gauss point  $k$  located in the volume  $V_r$ .  $\det(J_k)$  and  $W_k$  are the Jacobian determinant (relating to the differential area of the deformed element to the differential area of the master element) and weight function of the Gaussian quadrature rule at gauss point  $k$ . From the average Cauchy stress tensor, other stresses such as the principal stresses or the von Mises equivalent stress can be calculated.

Fig. 13 shows an example of the evolution of the average values of  $\sigma_{33}$ ,  $\epsilon_{33}$ , the von Mises equivalent stress and the accumulated plastic strain at a “hot-spot” (point  $P$  on the pore illustrated in Fig. 12) at loads corresponding to the macroscopic high-cycle fatigue strength.

It can be seen that without averaging, the local value of the von Mises stress at point  $P$  is approximately 210 MPa and the total strain amplitude is  $\epsilon_{33,a} \approx 0.3\%$ . For comparison, the cyclic hardening tests conducted on alloy C (i.e. the porosity-free alloy with a microstructure similar to alloy B) at this strain level had fatigue lives lower than  $10^4$  cycles. Hence, the high strain level at the “hot-spot” can explain early failures in the aluminium microstructure around pores and thus the rapid crack initiation (often less than  $10^4$  cycles) that has been widely observed in cast aluminium alloys even in the HCF regime [10,27]. It is also important to note that by using an averaging methodology, the plastic strain is lower and the mechanical response becomes essentially elastic for volumes of radius  $r = 40\text{--}60 \mu\text{m}$ .

From the average Cauchy stress tensor calculated at all gauss points surrounding the pore and at each step  $t$  in the loading cycle, a fatigue approach based on the Dang Van criterion [32] is proposed. The classical formulation of the Dang Van criterion is given by:

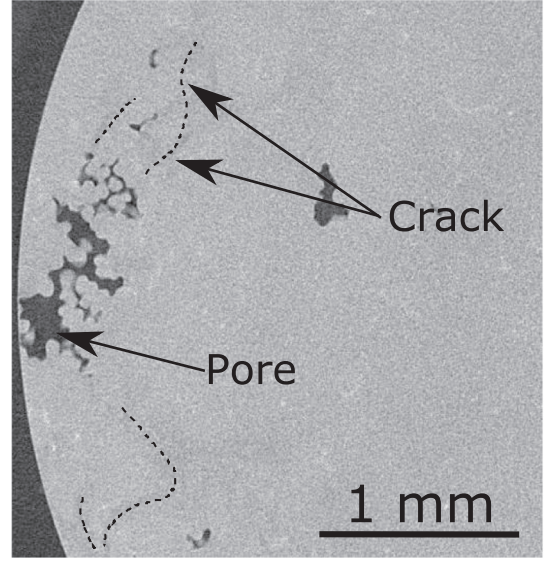


Fig. 10. An example of crack initiation from the critical pore of the specimen number 11 that intersect the specimen surface, observed by X-ray micro-tomography.

$$\max_{\underline{n}} (\max_{t \in T} [|\langle \hat{\underline{\underline{\tau}}}(\underline{n}, t) \rangle| + \alpha \langle \hat{\sigma}_H(t) \rangle]) < \beta \quad (7)$$

where  $\hat{\underline{\underline{\tau}}}(\underline{n}, t)$  is the mesoscopic shear stress vector acting on the slip plane  $\underline{n}$  for time  $t$  and  $\hat{\sigma}_H(t)$  is the mesoscopic hydrostatic pressure.  $T$  is the time period of the loading cycle.  $\alpha$  and  $\beta$  are two material parameters. Based on this formulation, an Dang Van equivalent stress is defined and the calculation of the average value of this stress is given by Eq. (8)

$$\langle \sigma_{DV,i} \rangle \Big|_r = \max_{\underline{n}} (\max_{t \in T} [|\langle \hat{\underline{\underline{\tau}}}(\underline{n}, t) \rangle|_r + \alpha \langle \hat{\sigma}_H(t) \rangle|_r]) \quad (8)$$

The average resolved shear stress  $\langle \hat{\underline{\underline{\tau}}}(\underline{n}, t) \rangle|_r$  and the average hydrostatic stress  $\langle \hat{\sigma}_H(t) \rangle|_r$  are calculated from the average Cauchy stress tensor  $\langle \underline{\underline{\sigma}}(t)_i \rangle|_r$ . The Dang Van coefficient  $\alpha$  is taken to be equal to 0.205. This value was identified from the fully reversed tension-compression fatigue strength and the fully reversed fatigue strength in torsion of alloy C (i.e. the porosity-free alloy) [10]. Finally, the Dang Van fatigue indicator is given by Eq. (9). Note that when this parameter is greater than or equal to one ( $DV \geq 1.0$ ), failure is predicted.

$$DV = \max_{i \in \Omega} \frac{\langle \sigma_{DV,i} \rangle|_r}{\beta} \quad (9)$$

where  $\beta = 72 \text{ MPa}$  is equal to the torsional fatigue strength of alloy C ( $R = -1$ ) [10].  $\Omega$  is the set of all gauss points surrounding the pore. This set contains the gauss points of all elements with at least one node on the pore surface.

In order to determine the optimum radius  $r$  for the averaging volume  $V_r$  which results in the best prediction of the macroscopic fatigue strength, the critical pore cumulated probability of occurrence (i.e. pores at the origin of the crack initiations) is calculated. Fig. 14 shows the evolution of this probability as a function of the Dang Van fatigue danger indicator,  $DV$ . The danger indicator,  $DV$  is calculated for two different sized averaging volumes  $V_r$ :  $r = 40 \mu\text{m}$  and  $r = 60 \mu\text{m}$ .

It can be seen that the  $r = 40 \mu\text{m}$  curves passes through the point where the Dang Van indicator equals one ( $DV = 1$ ) and the accumulated probability of occurrence is 50%, while for the  $r = 60 \mu\text{m}$  curve this value is approximately 95%. Thus, the radius  $r = 40 \mu\text{m}$  is chosen to best predict the macroscopic fatigue strength.

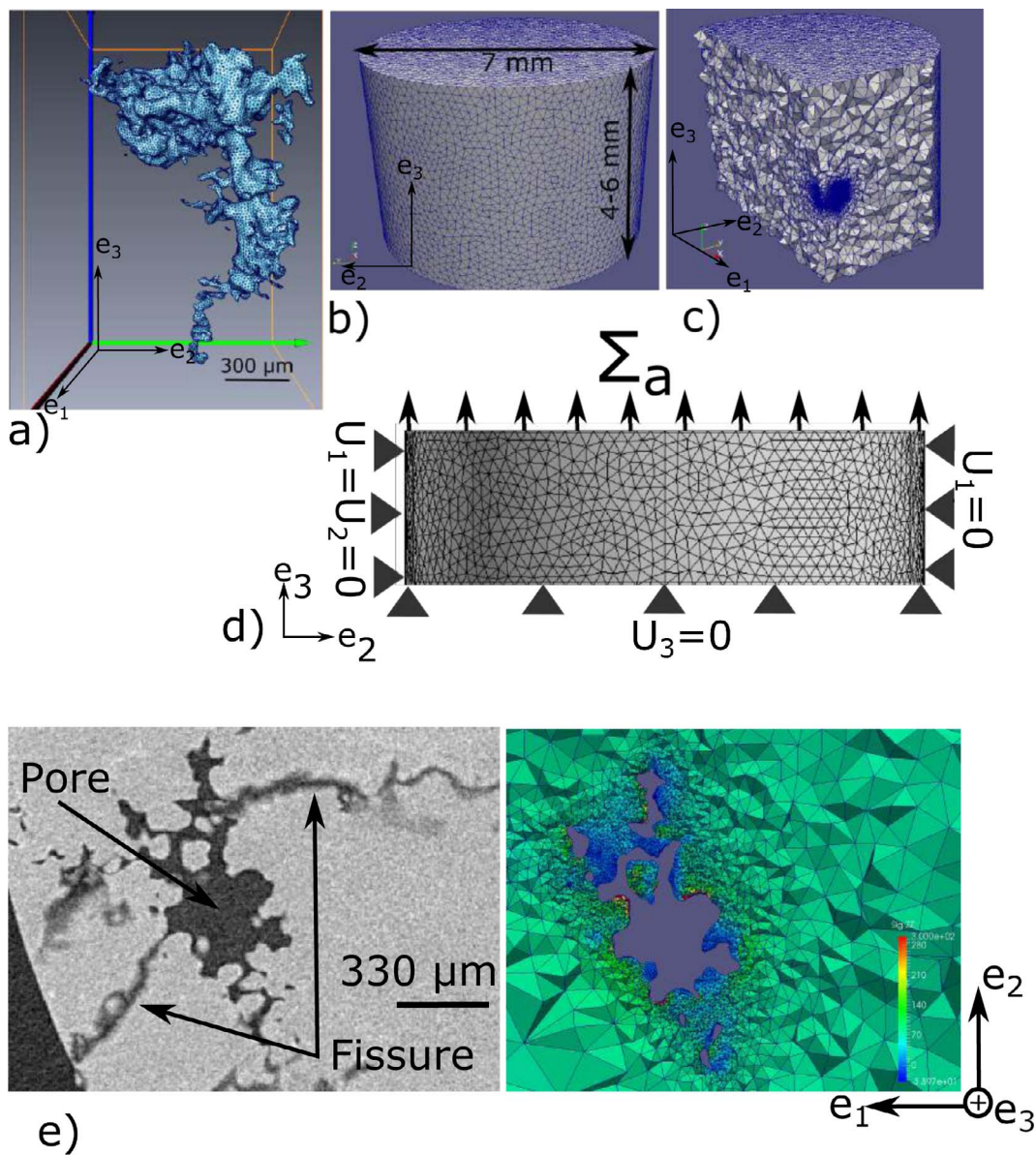


Fig. 11. Description of the FE models: (a) meshed surface of a pore, (b) meshed volume, (c) cut volume showing the pore and the volume mesh surrounding the pore, (d) boundary conditions, (e)  $e_1$ - $e_2$  cut plan showing an image obtained by micro-tomography of the critical pore of the specimen number 14 and the  $\sigma_{33}$  stress field surrounding the pore.

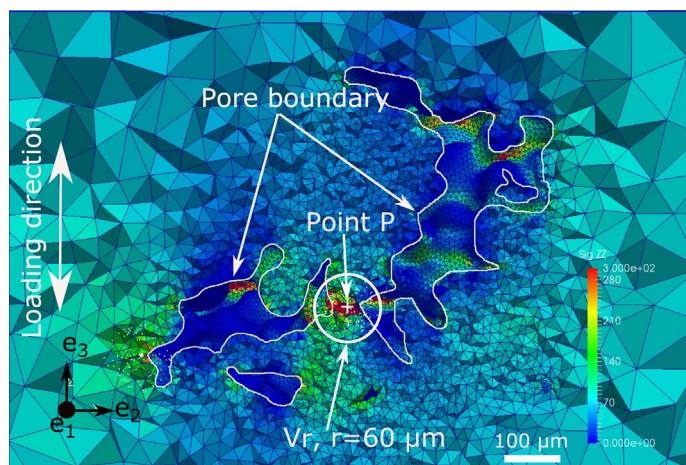
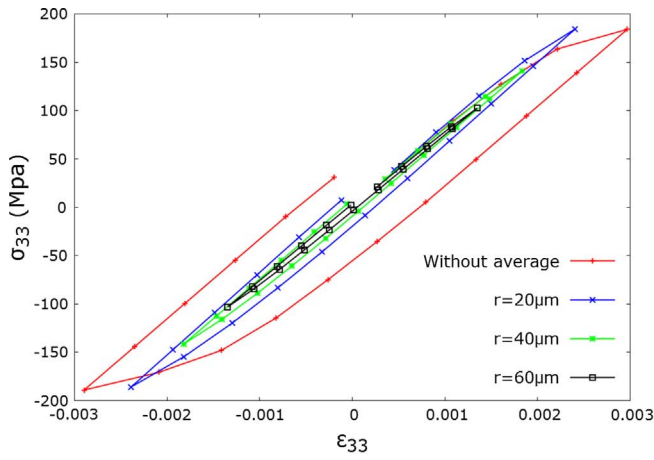
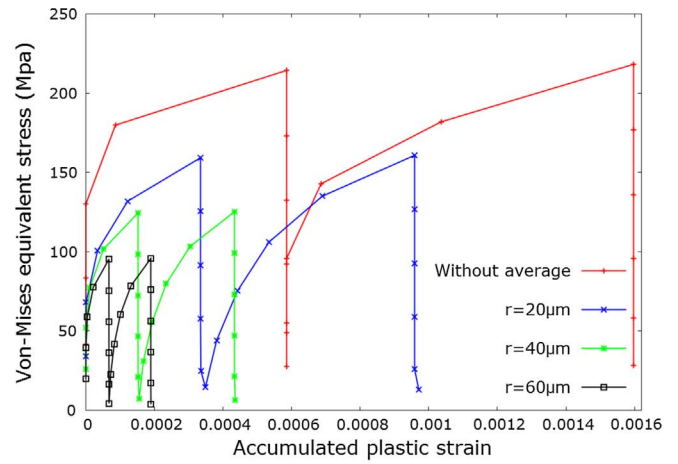


Fig. 12. A section through a pore of the specimen number 14 in the  $e_2$ - $e_3$  plane showing the 3D stress field as well as the position of a "hot-spot", marked point  $P$  and the volume  $V_r$  in which the average Cauchy stress tensor is assessed. The applied macroscopic stress amplitude is  $\Sigma_{33,a} = 70$  MPa.



(a)



(b)

Fig. 13. The mechanical response at point  $P$  for volumes of different radii  $V_r$ . (a) Stress-strain curves in the loading direction. (b) von Mises stress vs accumulated plastic strain curves. The applied macroscopic stress amplitude is  $\Sigma_{33,a} = 70$  MPa.

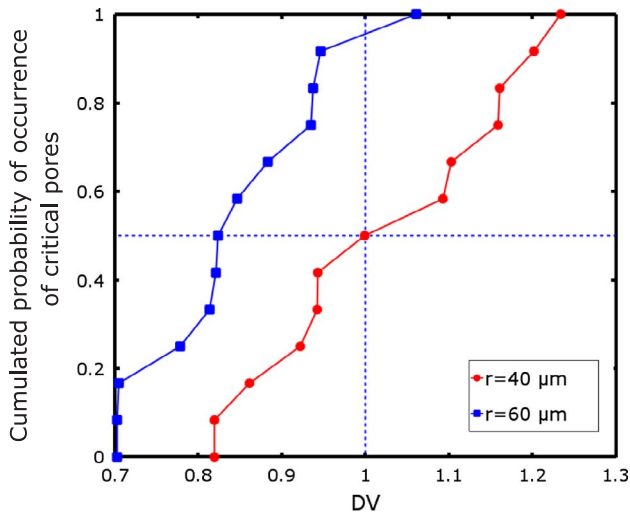


Fig. 14. Critical pores cumulative probability of occurrence as a function of the Dang Van fatigue indicator,  $DV$ , for two radii  $r$  of the average volume  $V_r$ .

#### 4.3. Prediction of the macroscopic fatigue strength and comparison with the experimental data

The proposed fatigue approach is used to predict the macroscopic fatigue strength of the 7 specimens shown in Table 3. The aim is to determine the macroscopic applied stress amplitude  $\Sigma_a$  for which the Dang Van fatigue indicator is equal to one ( $DV = 1$ ) for a averaging volume with a radius of  $r = 40 \mu\text{m}$ , around the pore initiating the principal fatigue crack (see Eq. (9)).

Fig. 15 shows the comparison between the predicted and experimentally determined fatigue strength of each specimen. The experimental fatigue strengths at  $2 \times 10^6$  cycles are determined by the following procedure [6]:

- For specimens loaded at several load levels before failure, the fatigue strength at  $2 \times 10^6$  cycles is determined by Eq. (10)

$$\Sigma_{a,D} = \Sigma_{a,n_f-1} + \frac{N_f}{2.10^6} \times (\Sigma_{a,n_f} - \Sigma_{a,n_f-1}) \quad (10)$$

where  $\Sigma_{a,D}$  is the fatigue strength,  $\Sigma_{a,n_f}$  is the applied stress amplitude level at the final step.

- For specimens that failed during the first load level, the Basquin equation (Eq. (11)) is used to determine the fatigue strength at

$2 \times 10^6$  cycles.

$$\Sigma_{a,D} = CN_f^{1/b} \quad (11)$$

where  $C$  and  $b$  are the Basquin constants. The Basquin slope parameter was identified for alloy B in previous work to be  $b = -5$  [10].

It can be seen in Fig. 15(a) that the proposed approach predicts a decrease in the fatigue strength with an increase in the equivalent pore size  $V^{1/3}$  that is in agreement with approaches at the macroscopic scale [2,6,11]. The difference between the numerical predictions and the experimental data is generally less than 15% (Fig. 15(b)).

In the next section, the effect of pore morphology on the local mechanical response is studied. The Dang Van equivalent stress is assessed for real casting pores and compared to several simplified pore geometries.

#### 4.4. Effect of pore morphology

Two simplified pore geometries are considered: a “spherical pore” and an “oblate spheroidal pore” with a major axis equal to 4 times the minor axis. The factor of 4 is arbitrarily chosen. These defects are introduced in the center of cylindrical matrix (diameter = 7 mm, height = 4 mm). Fig. 16 shows the geometry of these two pores. Note that the loading direction is  $e_3$ .

Concerning the real casting pores, in order to obtain a statistically representative result, 87 critical and non-critical pores were modelled. These pores are the largest pores observed by micro-tomography, located near the specimen surface (with a distance to the surface of less than 500  $\mu\text{m}$ ).

The normalized Dang Van equivalent stress “averaged” in spheres  $V_r$  of radius of 40  $\mu\text{m}$ , defined by Eq. (12), is used to compare the local mechanical response of the different pores.

$$\text{Normalised Dang Van stress} = \max_{i \in \Omega} \frac{\langle \sigma_{DV,i} \rangle_{r=40\mu\text{m}}}{\Sigma_a} \quad (12)$$

where  $\Sigma_a$  is the macroscopic applied stress and  $\Omega$  is the set of the gauss points surrounding the pore.

Fig. 17 shows the comparison of the normalized average Dang Van stress as a function of the equivalent pore size  $V^{1/3}$  for the real casting pores and the simplified pore geometries. The linear regression line in log-log space and the 95% confidence bands for the real casting pores are also shown.

It can be seen that the slope of the power trendline fitted to the real casting pores is higher than the slope of the trendline for the spherical

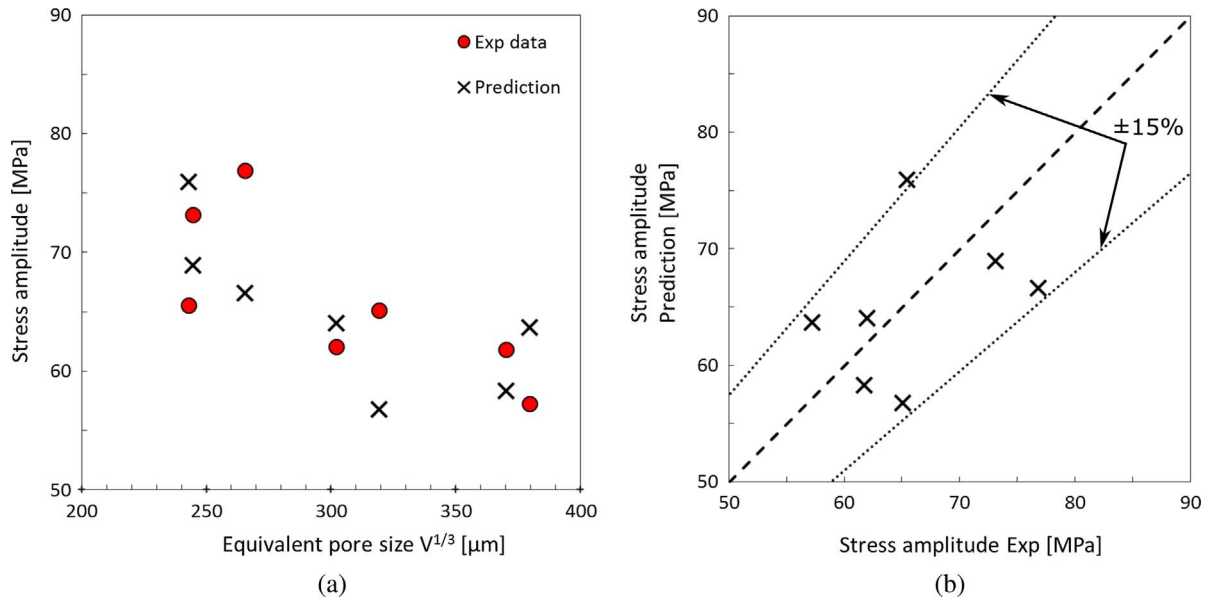


Fig. 15. Comparison between the predicted and the experimentally determined fatigue strengths of the 7 specimens shown in Table 3. (a) Fatigue strength amplitude as a function of pore size, (b) the predicted fatigue strength versus the experimental fatigue strength. The dotted lines show the margins of error of  $\pm 15\%$ .

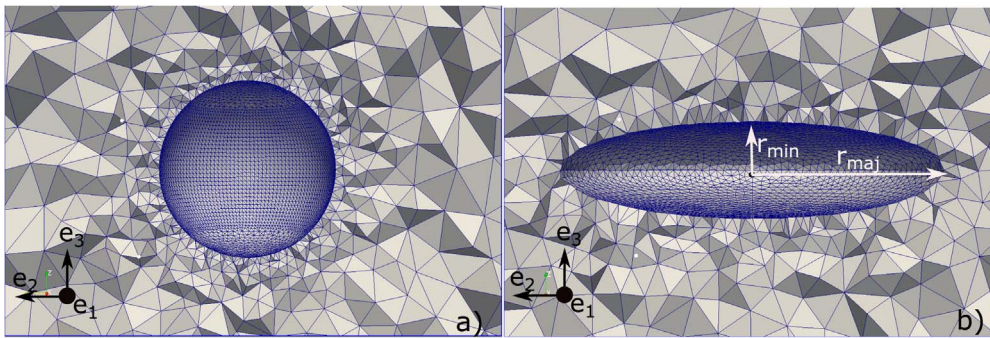


Fig. 16. Two simplified geometries: (a) spherical pore (sphericity = 1); (b) oblate spheroidal pore with  $r_{maj} = 4 \times r_{min}$  (sphericity  $\approx 0.7$ ). The loading direction is  $e_3$ .

pores. In other words, the effect of pore size on the normalized Dang Van stress is more pronounced for the real casting pores. This conclusion suggests that the effect of pore size on the fatigue strength is more detrimental for casting pores than the spherical pores. This prediction is

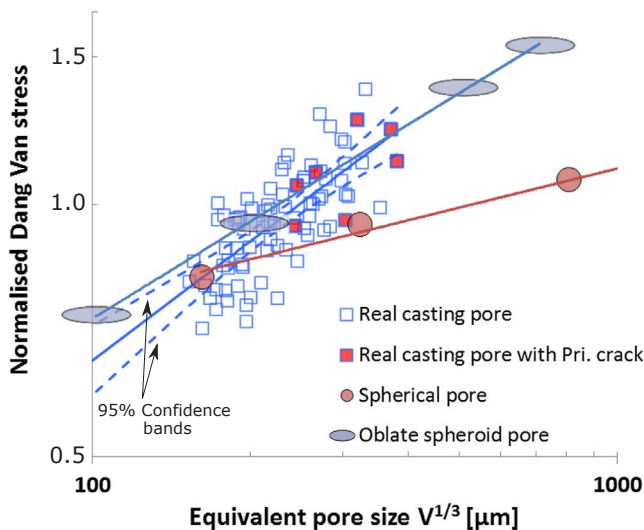


Fig. 17. Comparison of the local mechanical response of real casting pores and simplified pore geometries.

confirmed by the recent work of Dezecot et al. [33]. These authors showed via high resolution micro-tomography observations conducted on low cycle fatigue test of a cast aluminium alloy, that spherical pores (degassing pores) are less detrimental than tortuous pores (micro-shrinkage pore) of the same size. Concerning the “oblate spheroidal pores”, it is observed in Fig. 17 that the slope of the trendline is much closer to the slope of the real casting pores. However, in order to better correlate the slope of the real casting pores, simplified geometries with shaper shapes will be simulated in future work.

## 5. Conclusion

The X-ray micro-tomography technique was used to investigate the fatigue behaviour of an AlSi7Mg0.3 aluminium alloy obtained by the lost foam casting process. It was observed that, in addition to the pore size, the distance to the specimen surface plays a significant role in the initiation and propagation of fatigue cracks. All pores causing the initiation of principal fatigue cracks were located close to the specimen surface (with the distance to the surface less than  $500 \mu\text{m}$ ) even though larger internal pores were observed in the volume.

From the numerically scanned pore geometries obtained by the micro-tomography observations, 3D finite element simulations were conducted to investigate the local mechanical response surrounding the real pores. An elasto-plastic material behaviour model was used to describe the aluminium matrix. In order to identify the elasto-plastic constitutive equations, including non-linear isotropic and kinematic

hardening, cyclic hardening tests were conducted on the same porosity-free cast Al-Si alloy (obtained via a HIP treatment). The behaviour model was identified by an inverse optimization algorithm.

The finite element simulations showed that stress concentrations at the pores are very high and lead to local plasticity. In order to predict the fatigue strength, a critical volume approach was proposed that is based on the averaged values of the Dang Van criterion in a spherical volume of radius 40 µm. The radius of the critical volume has been determined via an inverse methodology. Good agreement between the predictions and the experimental data is obtained with errors of less than 15%). The influence of the pore geometry/morphology was also investigated. The proposed approach predicts a pore size sensitivity to the fatigue strength more significant for the real casting pores than for the spherical pores. For the oblate spheroidal pores with  $r_{maj.ax} = 4 \times r_{min.ax}$ , a similar pore size sensitivity to the fatigue strength comparing to the real pores is suggested. The approach used to model the fatigue strength of Alloy B can also be applied to Alloy A (AlSi7Cu05Mg03). However, the elasto-plastic constitutive equations must be re-identified because Alloy A contains copper, which modifies the mechanical response of the material microstructure.

## Acknowledgement

This work was financially supported by PSA Peugeot Citroën.

## References

- [1] Koutiri I, Bellett D, Morel F, Augustins L, Adrien J. High cycle fatigue damage mechanisms in cast aluminium subject to complex loads. *Int J Fatigue* 2013;47:44–57. <http://dx.doi.org/10.1016/j.ijfatigue.2012.07.008> <<http://www.sciencedirect.com/science/article/pii/S0142112312002356>> .
- [2] McDowell D, Gall K, Horstemeyer M, Fan J. Microstructure-based fatigue modeling of cast a356-t6 alloy. *Eng Fract Mech* 2003;70(1):49–80. [http://dx.doi.org/10.1016/S0013-7944\(02\)00021-8](http://dx.doi.org/10.1016/S0013-7944(02)00021-8) <<http://www.sciencedirect.com/science/article/pii/S0013794402000218>> .
- [3] Wang Q, Apelian D, Lados D. Fatigue behavior of a356-t6 aluminum cast alloys. Part I. Effect of casting defects. *J Light Met* 2001;1(1):73–84. [http://dx.doi.org/10.1016/S1471-5317\(00\)00008-0](http://dx.doi.org/10.1016/S1471-5317(00)00008-0) <<http://www.sciencedirect.com/science/article/pii/S1471531700000080>> .
- [4] Roy M, Nadot Y, Nadot-Martin C, Bardin P-G, Maijer D. Multiaxial kitagawa analysis of a356-t6. *Int J Fatigue* 2011;33(6):823–32. <http://dx.doi.org/10.1016/j.ijfatigue.2010.12.011> <<http://www.sciencedirect.com/science/article/pii/S0142112310003129>> .
- [5] Roy M, Nadot Y, Maijer DM, Benoit G. Multiaxial fatigue behaviour of a356-t6. *Fatigue Fract Eng Mater Struct* 2012;35(12):1148–59. <http://dx.doi.org/10.1111/j.1460-2695.2012.01702.x>.
- [6] Houria MI, Nadot Y, Fathallah R, Roy M, Maijer DM. Influence of casting defect and (SDAS) on the multiaxial fatigue behaviour of a356-t6 alloy including mean stress effect. *Int J Fatigue* 2015. <http://dx.doi.org/10.1016/j.ijfatigue.2015.05.012> <<http://www.sciencedirect.com/science/article/pii/S0142112315001619>> .
- [7] Koutiri I, Bellett D, Morel F, Pessard E. A probabilistic model for the high cycle fatigue behaviour of cast aluminium alloys subject to complex loads. *Int J Fatigue* 2013;47:137–47. <http://dx.doi.org/10.1016/j.ijfatigue.2012.08.004> <<http://www.sciencedirect.com/science/article/pii/S0142112312002472>> .
- [8] Brochu M, Verreman Y, Ajersch F, Bouchard D. High cycle fatigue strength of permanent mold and rheocast aluminum 357 alloy. *Int J Fatigue* 2010;32(8):1233–42. <http://dx.doi.org/10.1016/j.ijfatigue.2010.01.001> <<http://www.sciencedirect.com/science/article/pii/S0142112310000149>> .
- [9] Wang Q, Apelian D, Lados D. Fatigue behavior of a356/357 aluminum cast alloys. part (II) - effect of microstructural constituents. *J Light Met* 2001;1(1):85–97. [http://dx.doi.org/10.1016/S1471-5317\(00\)00009-2](http://dx.doi.org/10.1016/S1471-5317(00)00009-2) <<http://www.sciencedirect.com/science/article/pii/S1471531700000092>> .
- [10] Le V-D, Morel F, Bellett D, Saintier N, Osmond P. Multiaxial high cycle fatigue damage mechanisms associated with the different microstructural heterogeneities of cast aluminium alloys. *Mater Sci Eng: A* 2016;649:426–40. <http://dx.doi.org/10.1016/j.msea.2015.10.026> <<http://www.sciencedirect.com/science/article/pii/S0921509315304901>> .
- [11] Le V-D, Morel F, Bellett D, Saintier N, Osmond P. Simulation of the kitagawa-takahashi diagram using a probabilistic approach for cast al-si alloys under different multiaxial loads. *Int J Fatigue* 2016;93(Part 1):109–21. <http://dx.doi.org/10.1016/j.ijfatigue.2016.08.014> <<http://www.sciencedirect.com/science/article/pii/S014211231630247X>> .
- [12] Serrano-Munoz I, Buffière J-Y, Verdu C, Gaillard Y, Mu P, Nadot Y. Influence of surface and internal casting defects on the fatigue behaviour of a357-t6 cast aluminium alloy. *Int J Fatigue* 2016;82(Part 3):361–70. <http://dx.doi.org/10.1016/j.ijfatigue.2015.07.032> <<http://www.sciencedirect.com/science/article/pii/S0142112315002509>> .
- [13] Iben Houria M. Etude expérimentale et modélisation de la dure de vie en fatigue d'un alliage d'aluminium de fonderie a356-t6 sous chargement multiaxial [Ph.D. thesis]. ENSMA, 2015ESMA0007; 2015. <<http://www.theses.fr/2015ESMA0007>> .
- [14] Gao Y, Yi J, Lee P, Lindley T. A micro-cell model of the effect of microstructure and defects on fatigue resistance in cast aluminum alloys. *Acta Mater* 2004;52(19):5435–49. <http://dx.doi.org/10.1016/j.actamat.2004.07.035> <<http://www.sciencedirect.com/science/article/pii/S1359645404004446>> .
- [15] Fan J, McDowell DL, Horstemeyer MF, Gall K. Cyclic plasticity at pores and inclusions in cast alsi alloys. *Eng Fract Mech* 2003;70(10):1281–302. [http://dx.doi.org/10.1016/S0013-7944\(02\)00097-8](http://dx.doi.org/10.1016/S0013-7944(02)00097-8) <<http://www.sciencedirect.com/science/article/pii/S0013794402000978>> .
- [16] Ferri E, Buffière J-Y, Ludwig W, Gravouil A, Edwards L. Fatigue crack propagation: In situ visualization using X-ray microtomography and 3d simulation using the extended finite element method. *Acta Mater* 2006;54(4):1111–22. <http://dx.doi.org/10.1016/j.actamat.2005.10.053> <<http://www.sciencedirect.com/science/article/pii/S135964540500649X>> .
- [17] Ferri E, Buffière J-Y, Ludwig W. 3d characterisation of the nucleation of a short fatigue crack at a pore in a cast al alloy using high resolution synchrotron microtomography. *Int J Fatigue* 2005;27(10–12):1215–20. <http://dx.doi.org/10.1016/j.ijfatigue.2005.07.015>. fatigue Damage of Structural Materials V 5th International Conference on Fatigue Damage of Structural Materials. <<http://www.sciencedirect.com/science/article/pii/S0142112305001647>> .
- [18] Dezecot S, Buffière J-Y, Koster A, Maurel V, Szymka F, Charkaluk E, et al. In situ 3d characterization of high temperature fatigue damage mechanisms in a cast aluminium alloy using synchrotron X-ray tomography. *Scripta Mater* 2016;113:254–8. <http://dx.doi.org/10.1016/j.scriptamat.2015.11.017> <<http://www.sciencedirect.com/science/article/pii/S1359646215300579>> .
- [19] Nicoletto G, Anzelotti G, Konen R. X-ray computed tomography vs. metallography for pore sizing and fatigue of cast al-alloys. *Procedia Eng* 2010;2(1):547–54. <http://dx.doi.org/10.1016/j.proeng.2010.03.059>. fatigue 2010 <<http://www.sciencedirect.com/science/article/pii/S1877705810000603>> .
- [20] Nicoletto G, Konen R, Fintova S. Characterization of microshrinkage casting defects of alsi alloys by X-ray computed tomography and metallography. *Int J Fatigue* 2012;41:39–46. <http://dx.doi.org/10.1016/j.ijfatigue.2012.01.006> <<http://www.sciencedirect.com/science/article/pii/S0142112312000187>> .
- [21] Tijani Y, Heinrietz A, Bruder T, Hanselka H. Quantitative evaluation of fatigue life of cast aluminium alloys by non-destructive testing and parameter model. *Int J Fatigue* 2013;57:73–8. <http://dx.doi.org/10.1016/j.ijfatigue.2013.05.017> fatigue and Microstructure: A special issue on recent advances <<http://www.sciencedirect.com/science/article/pii/S0142112313001734>> .
- [22] Tijani Y, Heinrietz A, Stets W, Voigt P. Detection and influence of shrinkage pores and nonmetallic inclusions on fatigue life of cast aluminum alloys. *Metall Mater Trans A* 2013;44(12):5408–15. <http://dx.doi.org/10.1007/s11661-013-1773-0>.
- [23] Vanderesse N, Buffière J-Y, Maire E, Chabod A. Effect of porosity on the fatigue life of a cast Al alloy. *New York, NY: Springer New York*; 2011. p. 55–61. [http://dx.doi.org/10.1007/978-1-4614-0228-2\\_8](http://dx.doi.org/10.1007/978-1-4614-0228-2_8).
- [24] Feaugas X, Gaudin C. Ratchetting process in the stainless steel AISI 316l at 300 k: an experimental investigation. *Int J Plast* 2004;20(4–5):643–62. [http://dx.doi.org/10.1016/S0749-6419\(03\)00076-7](http://dx.doi.org/10.1016/S0749-6419(03)00076-7).
- [25] Lemaitre J, Chaboche J, Benallal A, Desmorat R. Mécanique des matériaux solides - 3ème édition, Physique, Dunod; 2009. <<https://books.google.fr/books?id=6kwLkhEc8cYC>> .
- [26] Borbély A, Mughrabi H, Eisenmeier G, Höppl H. A finite element modelling study of strain localization in the vicinity of near-surface cavities as a cause of subsurface fatigue crack initiation. *Int J Fract* 2002;115(3):227–32. <http://dx.doi.org/10.1023/A:1016350528652>.
- [27] Buffière J-Y, Savelli S, Jouneau P, Maire E, Fougères R. Experimental study of porosity and its relation to fatigue mechanisms of model alsi7mg0.3 cast al alloys. *Mater Sci Eng: A* 2001;316(1–2):115–26. [http://dx.doi.org/10.1016/S0921-5093\(01\)01225-4](http://dx.doi.org/10.1016/S0921-5093(01)01225-4) <<http://www.sciencedirect.com/science/article/pii/S0921509301012254>> .
- [28] Petit J, Henaff G, Sarrazin-Baudoux C. Environmentally assisted fatigue in the gaseous atmosphere. *Compr Struct Integr* 2003;6:211–80.
- [29] Susmel L, Taylor D. The theory of critical distances as an alternative experimental strategy for the determination of kic and kth. *Eng Fract Mech* 2010;77(9):1492–501. <http://dx.doi.org/10.1016/j.engfractmech.2010.04.016> <<http://www.sciencedirect.com/science/article/pii/S001379441000202X>> .
- [30] Bellett D, Taylor D, Marco S, Mazzeo E, Guillois J, Pircher T. The fatigue behaviour of three-dimensional stress concentrations. *Int J Fatigue* 2005;27(3):207–21. <http://dx.doi.org/10.1016/j.ijfatigue.2004.07.006> <<http://www.sciencedirect.com/science/article/pii/S0142112304001616>> .
- [31] El mayM. Etude de la tenue en fatigue d'un acier inoxydable pour l'aronautique en milieu marin corrosif [Ph.D. thesis]; 2013. <<http://www.theses.fr/2013ENAM0012/document>> .
- [32] DangVan. Sur la resistance a la fatigue des metaux. *Sciences et techniques de l'armement* 1973(47):641–772.
- [33] Dezecot S, Maurel V, Buffière J-Y, Szymka F, Koster A. 3d characterization and modeling of low cycle fatigue damage mechanisms at high temperature in a cast aluminium alloy. *Acta Mater* 2017;123:24–34. <http://dx.doi.org/10.1016/j.actamat.2016.10.028> <<http://www.sciencedirect.com/science/article/pii/S1359645416307923>> .